

Magnetic resonance imaging appropriate for construction of subject-specific head models for diffuse optical tomography

Kazuki Kurihara,¹ Hiroshi Kawaguchi,^{2,3} Takayuki Obata,^{3,4} Hiroshi Ito,^{3,5}
and Eiji Okada^{1,*}

¹Department of Electronics and Electrical Engineering, Keio University, 3-14-1 Hiyoshi, Kohoku-ku, Yokohama, 223-8522, Japan

²Human Informatics Research Institute, National Institute of Advanced Industrial Science and Technology, Central 6, 1-1-1 Higashi, Tsukuba, Ibaraki, 305-8566, Japan

³Molecular Imaging Center, National Institute of Radiological Sciences, 4-9-1 Anagawa, Inage-ku, Chiba, 263-8555, Japan

⁴Research Center for Charged Particle Therapy, National Institute of Radiological Sciences, 4-9-1 Anagawa, Inage-ku, Chiba, 263-8555, Japan

⁵Advanced Clinical Research Center, Fukushima Medical University, 1 Hikarigaoka, Fukushima, 960-1295, Japan
*okada@elec.keio.ac.jp

Abstract: Subject-specific head models of which their geometry is based on structural magnetic resonance images are essential to accurately estimate the spatial sensitivity profiles for image reconstruction in diffuse optical tomography. T1-weighted magnetic resonance images, which are commonly used for structural imaging, are not sufficient for the threshold-based segmentation of the superficial tissues. Two types of pulse sequences, which provide a high contrast among the superficial tissues, are introduced to complement the segmentation to construct the subject-specific head models. The magnetic resonance images acquired by the proposed pulse sequences are robust to the threshold level and adequate for the threshold-based segmentation of the superficial tissues compared to the T1- and T2-weighted images. The total scan time of the proposed pulse sequences is less than one-fourth of that for the T2-weighted pulse sequence.

©2015 Optical Society of America

OCIS codes: (170.2655) Functional monitoring and imaging; (170.3660) Light propagation in tissues.

References and links

1. A. Maki, Y. Yamashita, Y. Ito, E. Watanabe, Y. Mayanagi, and H. Koizumi, "Spatial and temporal analysis of human motor activity using noninvasive NIR topography," *Med. Phys.* **22**(12), 1997–2005 (1995).
2. H. Kawaguchi, T. Koyama, and E. Okada, "Effect of probe arrangement on reproducibility of images by near-infrared topography evaluated by a virtual head phantom," *Appl. Opt.* **46**(10), 1658–1668 (2007).
3. B. R. White and J. P. Culver, "Quantitative evaluation of high-density diffuse optical tomography: *in vivo* resolution and mapping performance," *J. Biomed. Opt.* **15**(2), 026006 (2010).
4. Y. Fukui, Y. Ajichi, and E. Okada, "Monte Carlo prediction of near-infrared light propagation in realistic adult and neonatal head models," *Appl. Opt.* **42**(16), 2881–2887 (2003).
5. A. H. Bamett, J. P. Culver, A. G. Sorensen, A. Dale, and D. A. Boas, "Robust inference of baseline optical properties of the human head with three-dimensional segmentation from magnetic resonance imaging," *Appl. Opt.* **42**(16), 3095–3108 (2003).
6. K. Kurihara, H. Kawaguchi, T. Obata, H. Ito, K. Sakatani, and E. Okada, "The influence of frontal sinus in brain activation measurements by near-infrared spectroscopy analyzed by realistic head models," *Biomed. Opt. Express* **3**(9), 2121–2130 (2012).
7. Y. Zhan, A. T. Eggebrecht, J. P. Culver, and H. Dehghani, "Image quality analysis of high-density diffuse optical tomography incorporating a subject-specific head model," *Front. Neuroenergetics* **4**(6), 6 (2012).
8. A. T. Eggebrecht, B. R. White, S. L. Ferradal, C. Chen, Y. Zhan, A. Z. Snyder, H. Dehghani, and J. P. Culver, "A quantitative spatial comparison of high-density diffuse optical tomography and fMRI cortical mapping," *Neuroimage* **61**(4), 1120–1128 (2012).

9. M. Jermyn, H. Ghadyani, M. A. Mastanduno, W. Turner, S. C. Davis, H. Dehghani, and B. W. Pogue, "Fast segmentation and high-quality three-dimensional volume mesh creation from medical images for diffuse optical tomography," *J. Biomed. Opt.* **18**(8), 086007 (2013).
10. J. Ashburner, "SPM: A history," *Neuroimage* **62**(2), 791–800 (2012).
11. Y. Zhang, M. Brady, and S. Smith, "Segmentation of brain MR images through a hidden Markov random field model and the expectation-maximization algorithm," *IEEE Trans. Med. Imaging* **20**(1), 45–57 (2001).
12. M. Jenkinson, C. F. Beckmann, T. E. J. Behrens, M. W. Woolrich, and S. M. Smith, "FSL," *Neuroimage* **62**(2), 782–790 (2012).
13. S. M. Smith, "Fast robust automated brain extraction," *Hum. Brain Mapp.* **17**(3), 143–155 (2002).
14. S. Jenkinson, M. Pechaud, and S. Smith, "BET2: MR-based estimation of brain, skull and scalp surfaces," Eleventh Annual Meeting of the Organization for Human Brain Mapping (2005).
15. K. L. Perdue and S. G. Diamond, "T1 magnetic resonance imaging head segmentation for diffuse optical tomography and electroencephalography," *J. Biomed. Opt.* **19**(2), 026011 (2014).
16. P. J. Keller, W. W. Hunter, Jr., and P. Schmalbrock, "Multisection fat-water imaging with chemical shift selective presaturation," *Radiology* **164**(2), 539–541 (1987).
17. B. Schmitz, T. Hagen, and W. Reith, "Three-dimensional true FISP for high-resolution imaging of the whole brain," *Eur. Radiol.* **13**(7), 1577–1582 (2003).
18. M. Hiraoka, M. Firbank, M. Essenpreis, M. Cope, S. R. Arridge, P. van der Zee, and D. T. Delpy, "A Monte Carlo investigation of optical pathlength in inhomogeneous tissue and its application to near-infrared spectroscopy," *Phys. Med. Biol.* **38**(12), 1859–1876 (1993).
19. C. R. Simpson, M. Kohl, M. Essenpreis, and M. Cope, "Near-infrared optical properties of *ex vivo* human skin and subcutaneous tissues measured using the Monte Carlo inversion technique," *Phys. Med. Biol.* **43**(9), 2465–2478 (1998).
20. M. Firbank, M. Hiraoka, M. Essenpreis, and D. T. Delpy, "Measurement of the optical properties of the skull in the wavelength range 650–950 nm," *Phys. Med. Biol.* **38**(4), 503–510 (1993).
21. E. Okada and D. T. Delpy, "Near-infrared light propagation in an adult head model. I. Modeling of low-level scattering in the cerebrospinal fluid layer," *Appl. Opt.* **42**(16), 2906–2914 (2003).
22. P. van der Zee, M. Essenpreis, and D. T. Delpy, "Optical properties of brain tissue," *Proc. SPIE* **1888**, 454–465 (1993).

1. Introduction

Near-infrared spectroscopy and imaging have been applied to measure the hemodynamic response related to brain activation. The concentration change in hemoglobin in the brain is measured as the change in intensity detected by source-detector pairs attached to the scalp surface. Light is strongly scattered in the tissues and the detected light propagates through a broad region in the head. Near infrared topography can visualize the brain activation from the change in intensity detected by multiple probe pairs without information about light propagation in the head [1]. The measured data are mapped to the midpoint of the corresponding probe pair and the data are interpolated to obtain the brain function image. The limitation of the spatial resolution of near infrared topography is caused by the sparse probe arrangement and a broadened spatial sensitivity of the probe pairs [2]. Diffuse optical tomography (DOT) employing the high-density probe arrangement and image reconstruction algorithm incorporating the spatial sensitivity profile effectively improves the spatial resolution of the brain function image [3].

It is necessary to model light propagation in the head to estimate the spatial sensitivity profiles. Since the heterogeneity of the optical properties in the head affects light propagation in the brain, the model is typically segmented into five regions, i.e., the scalp, skull, cerebrospinal fluid (CSF), gray matter and white matter, and the geometry of the model is based on structural magnetic resonance (MR) images of the head [4–9]. The size of the head and the thickness of the superficial tissues vary among individuals and a subject-specific head model is preferred to accurately estimate the spatial sensitivity profiles. T1-weighted (T1W) is the most common pulse sequence of structural MR imaging and it has good contrast to segment the brain regions, i.e., the CSF, gray matter and white matter [10, 11]. In the DOT, light propagation in the brain is significantly affected by the thickness and geometry of the superficial tissues. Although the segmentation of the superficial tissues is very important, the T1W image provides almost no contrast between the skull and CSF. The skull/CSF boundary can be automatically extracted from only the T1W images by some software packages [12–15]. They do not directly find the boundary in the image, but estimate the boundary using

priori knowledge. It is better to additionally use the MR image which provides good contrast among the superficial tissues to precisely construct subject-specific head models.

The T2-weighted (T2W) pulse sequence is also commonly used in clinical applications and it provides a bright signal from the scalp and CSF, while a dark signal from the skull. The T1W and T2W images are a good pair to segment the anatomical images into the five types of tissues [14]. A disadvantage of the T2W image is its long scan time. The scan time of the T2W image is more than five times as long as that of the T1W image. A prolonged imaging imposes a strain on a subject and evokes a motion artifact.

In this study, two pulse sequences of the MR imaging, which provide a good contrast between the skull and CSF and between the CSF and gray matter, were evaluated in terms of adequacy to threshold-based segmentation of the superficial tissues to construct subject-specific head models for the DOT. The fat-saturated proton density weighted (FS-PDW) pulse sequence was selected for improvement of the contrast between the scalp and CSF. The proton density weighted (PDW) image provides a dark signal from the skull whereas a bright signal from the scalp and CSF, and a good contrast between the scalp and skull and between the skull and CSF [16]. The PDW image also provides a bright signal from yellow bone marrow in the skull and it reduces the contrast of the skull. In the FS-PDW, fat suppression was adopted to the PDW pulse sequence to suppress the signal from the yellow bone marrow. Fast imaging employing the steady-state acquisition (FIESTA) pulse sequence, in which the signal is related to the ratio of T2 to T1, can highlight the CSF. The FIESTA was selected to improve the contrast between the CSF and gray matter [17]. The MR images acquired by T1W, T2W, FS-PDW and FIESTA were segmented by a threshold-based segmentation algorithm to evaluate the adequacy of the MR images in order to extract the particular types of tissues and robustness of the threshold level. The MR images acquired by the proposed sequences were applied to the FMRIB software library (FSL) tools, which is designed for the T1W and T2W images, to evaluate the adaptivity to the publicly available segmentation tools. Three-dimensional whole head models were constructed from the MR images acquired by the T1W and T2W and by the FS-PDW, FIESTA and T1W. The light propagation in these models was compared to that in the manually segmented head model.

2. Method

2.1 Acquisition of MR images

Forty-six healthy volunteers (24 males and 22 females, 38.0 ± 11.4 years old) participated in this study. The study was approved by the Ethics and Radiation Safety Committees of the National Institute of Radiological Sciences, Chiba, Japan. All participants gave their written informed consent.

All the MR experiments were performed using a 3.0-T clinical MR system (SignaHDx 3.0; GE Healthcare, Milwaukee, WI, USA). The detailed scan parameters of the four contrast variant images are as follows:

- a) T1W, 3-dimensional spoiled gradient echo (3D-SPGR) with inversion pulse and array spatial sensitivity encoding technique (ASSET), repetition time (TR) / echo time (TE) / inversion time (TI) = 6.8/1.9/450 ms, flip angle (FA) = 12 degree, matrix = 256×256 , number of excitation (NEX) = 1;
- b) T2W, fast spin echo with flow compensation, transaxial plane, TR/TE = 4000/90 ms, echo train length = 16, matrix 512×512 , NEX = 2;
- c) FS-PDW, 3D-SPGR with ASSET and tailored radiofrequency pulse for FS, TR/TE = 13.8/1.9 ms, FA = 6 degree, matrix = 256×256 , NEX = 1;
- d) FIESTA, TR/TE = 13.8/1.9, FA = 45 degree, matrix = 256×256 , NEX = 1. ASSET factor of 2 was applied to all sequences using ASSET.

The field of view and slice thickness of all the images are 26.0 cm and 1.0 mm, respectively. The scan time for the MR image acquisition is shown in Table 1. The scan time for T2W was much longer than that for other image acquisitions. All the image data were anonymized before the segmentation process.

Table 1. Scan time for MR image acquisition.

	T1W	T2W	FS-PDW	FIESTA
scan time (s/slice)	1.21	6.96	1.35	0.31

2.2 Segmentation of tissues

2.2.1 Manual ground-truth segmentation

The whole head MR images of one subject were manually segmented into four regions, i.e. the scalp, skull, CSF, and brain, to create the most accurate ground-truth data of a 3D subject-specific head model. A slice of the MR image of the other 45 subjects was also manually segmented into the four regions to evaluate the between-subject reproducibility of the threshold-based segmentation.

2.2.2 Threshold-based segmentation

The MR images were segmented into the four regions, i.e., the scalp, skull, CSF and brain, using binarization and morphological operations to compare the suitability of the four contrast variant MR images to the threshold-based algorithms for the superficial tissue segmentation. The process to extract the scalp mask, outer skull mask, inner skull mask and brain mask is as follows:

- a) scalp mask (air/scalp boundary)
 - a-1) The MR image was binarized using the threshold level to segment the air and scalp.
 - a-2) Unextracted regions remaining inside the scalp were extracted by the closing operation.
- b) inner skull mask (skull/CSF boundary)
 - b-1) The MR image was binarized using the threshold level to segment the skull and CSF.
 - b-2) Extracted regions outside of the skull (mainly the scalp) were removed by the erosion operation.
 - b-3) The primary region (the inner skull mask) was selected by the labeling process.
 - b-4) Influence of the erosion operation on the mask was compensated by the dilation operation.
- c) outer skull mask (scalp/skull boundary)
 - c-1) The MR image was binarized using the threshold level to segment the scalp and skull.
 - c-2) The air region was removed using the scalp mask.
 - c-3) The inner skull mask was added to the extracted region.
 - c-4) Pepper noise in the mask was removed by the closing operation.
- d) brain mask (CSF/gray matter boundary)

d-1) The MR image was binarized using the threshold level to segment the CSF and gray matter.

d-2) Extracted regions outside the CSF (mainly the skull and air) were removed using the inner skull mask

d-3) Salt noise outside the mask was removed by the erosion operation.

d-4) The primary (brain) region was selected by the labeling process.

d-5) Influence of the erosion operation on the mask was compensated by the dilation operation.

The T1W, T2W and FS-PDW images were used to segment the scalp, outer skull and inner skull masks and the T1W, T2W and FIESTA images were used to segment the brain mask.

2.2.3 Segmentation by FSL tools

The segmentation of the MR images was also performed using FSL tools to evaluate the compatibility of the FS-PDW and FIESTA images to the publicly available segmentation tools.

The scalp and skull regions were segmented by the Brain Extraction Tool (BET). The BET is designed to estimate the air/scalp, scalp/skull and skull/CSF boundaries of the head from the T1W images or a pair of T1W and T2W images. The FS-PDW images were segmented to extract the scalp and skull regions by the BET.

The CSF/gray matter boundary was extracted by FMRIB's Automated Segmentation Tool (FAST). Before running the FAST, MR images were extracted by the inner skull mask and the MR images consisting of the CSF and brain regions were fed into the FAST. The number of classes to be segmented was two, and the images were segmented into the CSF and brain regions. The FIESTA images as well as the T1W and T2W images were segmented to estimate the CSF/gray matter boundary by the FAST.

2.3 Construction of head models and light propagation analysis

Light propagation in three whole-head models was obtained by the manual ground-truth segmentation and the threshold-based segmentation from two sets of MR head images. The scalp, outer skull and brain masks were segmented from the T1W images and the inner skull mask was segmented from the T2W images for the model by the previous set of pulse sequences. The scalp, outer skull and inner skull masks were segmented from the FS-PDW images and the brain mask was segmented from the FIESTA images for the model by the proposed set of pulse sequences. The brain region of all the models was segmented into the gray matter and white matter regions from the T1W images by the FAST.

The light propagation in the models was calculated by use of a previously described Monte Carlo method based on a variance reduction technique [18]. Each voxel in the models was specified with its optical properties according to the results of the segmentations. The optical properties of the five types of tissues in the head models are shown in Table 2. These values were chosen from the reported data for each type of tissue at the 830-nm wavelength [19–22]. The partial optical path length in the superficial tissues (the scalp and skull) and the brain (the gray matter and white matter) and the spatial sensitivity profiles estimated by the 3D head models obtained by the threshold-based segmentation were compared to those obtained by the manually segmented ground-truth model.

Table 2. The optical properties of tissues for light propagation analysis in the head models.

	transport scattering coefficient (mm ⁻¹)	absorption coefficient (mm ⁻¹)
scalp	1.84	0.025
skull	1.48	0.016
CSF	0.24	0.001
gray matter	2.12	0.039
white matter	8.82	0.017

3. Results and discussion

3.1 Threshold-based segmentation of MR images

A T1W image of a head and its pixel intensity histogram are shown in Figs. 1(a) and 1(b), respectively. In the T1W image, the scalp and white matter appear bright whereas the skull and CSF appear dark. The gray matter is darker than the white matter and brighter than the CSF. The contrast between the gray matter and white matter and between the gray matter and CSF seems adequate for the threshold-based segmentation. The histograms of the skull and CSF in the T1W image are completely overlapped indicating that the T1W images are not suitable for the threshold-based segmentation of the skull and CSF.

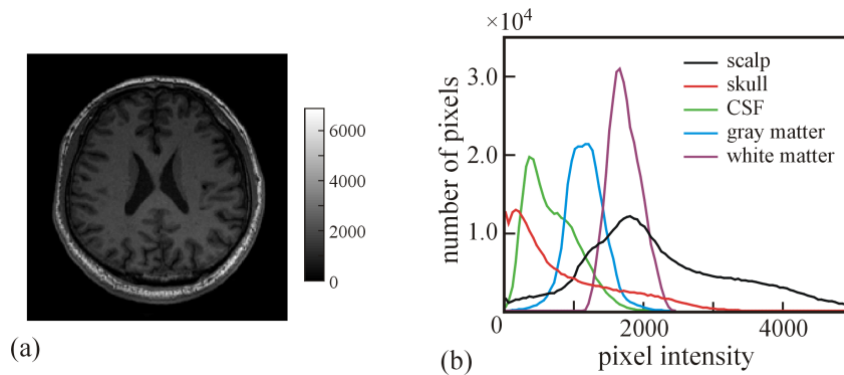


Fig. 1. T1W MR image of head: (a) Axial image, (b) image histogram.

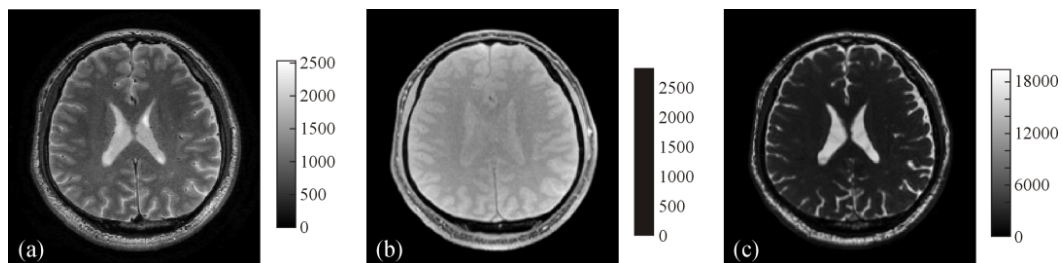


Fig. 2. MR images of head: (a) T2W, (b) FS-PDW, (c) FIESTA.

The MR head images acquired with T2W, FS-PDW and FIESTA are shown in Figs. 2(a), 2(b) and 2(c), respectively. In the T2W image, the scalp and CSF appear bright whereas the skull is dark. That is why the T2W images have been complementally used to segment the skull region. The FS-PDW image provides a bright signal from the scalp and brain whereas a dark signal from the skull including the yellow bone marrow as shown in Fig. 2(b). The contrast between the scalp and skull is higher than that of the T2W image. The CSF provides a bright signal whereas the skull and brain appear dark in the FIESTA image as shown in Fig. 2(c).

The scalp, outer skull and inner skull masks were segmented from the T1W, T2W and FS-PDW images and the brain mask were segmented from the T1W, T2W and FIESTA images.

In order to evaluate the robustness of the segmentation to the threshold level, the threshold level in the threshold-based segmentation was changed and the results of the segmentation were compared to the ground-truth image. The accuracy of the segmentation was quantified by the Dice coefficient, D , between the boundary mask obtained by the threshold-based segmentation and corresponding ground-truth image.

$$D = \frac{2|I_S \cap I_G|}{|I_S| + |I_G|} \quad (1)$$

where I_S and I_G are the segmented and ground-truth images, respectively. Figure 3 shows the relationship between the threshold level and Dice coefficient of the segmented images of (a) scalp mask, (b) outer skull mask, (c) inner skull mask and (d) brain mask. The segmentation of the scalp and outer skull masks from the T1W images is robust to the threshold level as well as that by the FS-PDW images as shown in Figs. 3(a) and 3(b). The skull/CSF boundary was not accurately segmented from the T1W images, and the results for the T2W and FS-PDW images are only shown in Fig. 3(c). Both the T2W and FS-PDW images are adequate to segment the skull/CSF boundary, however, the segmentation from the FS-PDW image is more robust to the threshold level and more accurate than that from the T2W image. The maximum value of the Dice coefficient for the brain mask is smaller than that for the other masks because the geometry of the CSF around the sulcus structure is complicated. The maximum values of Dice coefficient for the T1W, T2W and FIESTA images are almost the same, however, the threshold levels for the T1W and T2W images must be more precisely determined compared to the FIESTA images.

The scalp, outer skull and inner skull masks segmented from the T1W, T2W and FS-PDW images with the most appropriate threshold level and difference images between the images obtained by the threshold-based segmentation and the corresponding ground-truth images are shown in Fig. 4. In the difference images, the blue and red areas represent the false positive and false negative extractions, respectively. Appropriate boundary masks can be obtained from the T1W, T2W and FS-PDW images by the threshold-based segmentation with the optimal threshold level except for the inner skull mask from the T1W image.

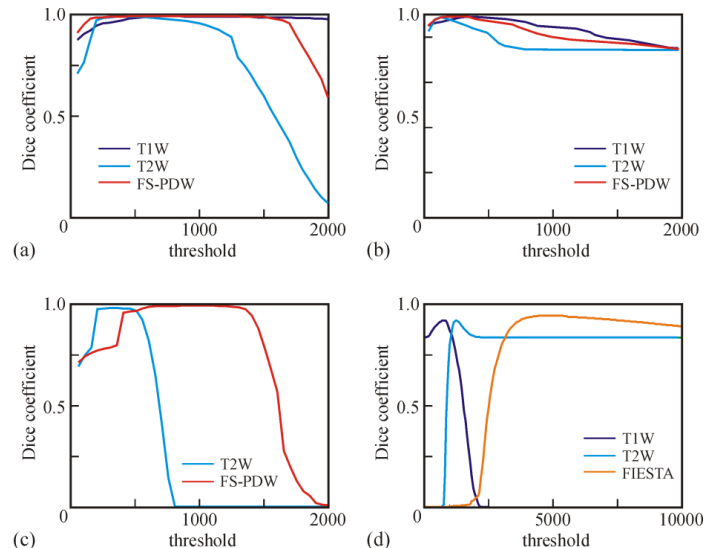


Fig. 3. Relationship between threshold and Dice coefficient of segmented image: (a) scalp mask, (b) outer skull mask, (c) inner skull mask, (d) brain mask.





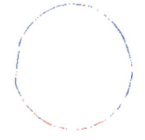
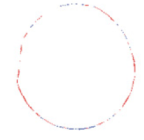
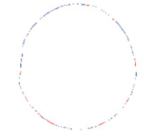




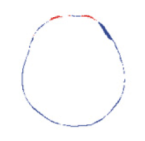

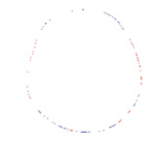




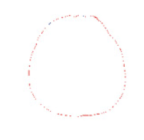
	ground-truth image	T1W	T2W	FS-PDW	
scalp mask					segmented image
					difference image
outer skull mask					segmented image
					difference image
inner skull mask		NA			segmented image
					difference image

Fig. 4. Segmented boundary masks of the scalp, outer skull and inner skull.






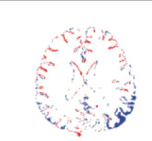
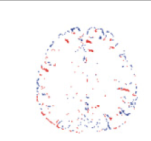
	ground-truth image	T1W	T2W	FS-PDW	
brain mask					segmented image
					difference image

Fig. 5. Segmented boundary masks of the brain.

The brain mask segmented from the T1W, T2W and FIESTA images with the most appropriate threshold level and difference images between the segmented images and the corresponding ground-truth images are shown in Fig. 5. The brain region is reasonably segmented from the three types of MR images, however, the segmentation error around the sulcus is more significant in the results from the T1W and T2W images compared to that from the FIESTA image.

A 3D subject-specific head model was constructed from the results of the segmentation. The scalp, skull, and CSF regions are obtained from the scalp and outer skull masks, the outer and inner skull masks, and the inner skull and brain masks, respectively. The gray matter/white matter boundary was obtained from the T1W image by the FAST. A frame from a movie ([Visualization 1](#)) of the transaxial plane of the 3D subject-specific head model obtained from the manual ground-truth segmentation and threshold-based segmentation from the MR images acquired by the proposed set of pulse sequences is shown in Fig. 6. As shown in the movie, the different tissue regions in the subject-specific head model are accurately obtained from the MR images by the threshold-based segmentation.

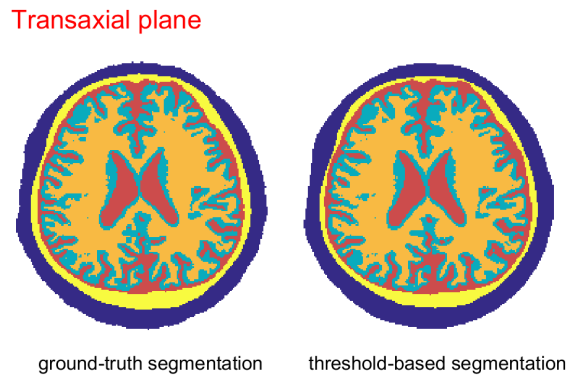


Fig. 6. Frame from a movie ([Visualization 1](#)) of the comparison of subject-specific head models obtained by the manual ground-truth segmentation and threshold-based segmentation.

The scalp, skull and CSF regions were segmented from a set of MR images in the transaxial plane of the other 45 subjects. The optimal threshold level was selected for each MR image for the MR images acquired by the conventional pulse sequences (T1W and T2W), whereas the threshold levels for the MR images acquired by the proposed pulse sequences (FS-PDW and FIESTA) were based on those optimized to the MR images for the 3D head model. The Dice coefficient between the regions in the superficial tissues obtained by the threshold-based segmentation from the MR images acquired by the two sets pulse sequences and the ground truth of those obtained by the manual segmentation were calculated for the 136 transaxial plane images in the 3D head model for a subject and a transaxial plane image for each of the 46 subjects, and the results are shown in Table 3. The Dice coefficients for the MR images acquired by the proposed pulse sequences are greater than those for the MR images acquired by the conventional pulse sequences. These results indicate that the FS-PDW and FIESTA images are robust to threshold level and appropriate for the threshold-based segmentation.

Table 3. Dice coefficient between segmented images and ground-truth image.

	3D head of a subject		a transaxial plane of 46 subjects	
	previous set of pulse sequences	proposed set of pulse sequences	previous set of pulse sequences	proposed set of pulse sequences
scalp	0.946	0.965	0.876 ± 0.054	0.900 ± 0.036
skull	0.883	0.940	0.812 ± 0.052	0.862 ± 0.038
CSF	0.747	0.852	0.700 ± 0.064	0.735 ± 0.071

3.2 Segmentation by FSL

The scalp and skull regions segmented from the T1W, pair of T1W and T2W, and FS-PDW by the BET and the difference images between the segmented images and the corresponding ground-truth images are shown in Fig. 7. The blue and red areas in the difference images represent the false positive and false negative extractions, respectively. The accuracy of the segmented scalp regions obtained from the T1W, T2W and FS-PDW is almost the same. The shapes of the skull regions segmented from the three types of MR images seem reasonable, however, a significant error in the segmentation is observed in the difference image for the T1W image. In the segmented images obtained from the pair of T1W and T2W images, the segmentation error is significantly reduced compared to that obtained from the T1W image except for only the frontal and occipital regions. Although the skull region segmented from the FS-PDW images is slightly thinner than the ground truth all around, the result is more accurate than those segmented from T1W and T2W.

The CSF region segmented from the T1W, T2W, and FIESTA by the FAST and the difference images between the segmented images and their ground truth are shown in Fig. 8. Since the outer boundary of the CSF was extracted before running the FAST, the skull/CSF boundaries of all the segmented images are the same. The CSF region segmented from the FIESTA by the FAST is almost the same as that segmented from the T1W and T2W images.

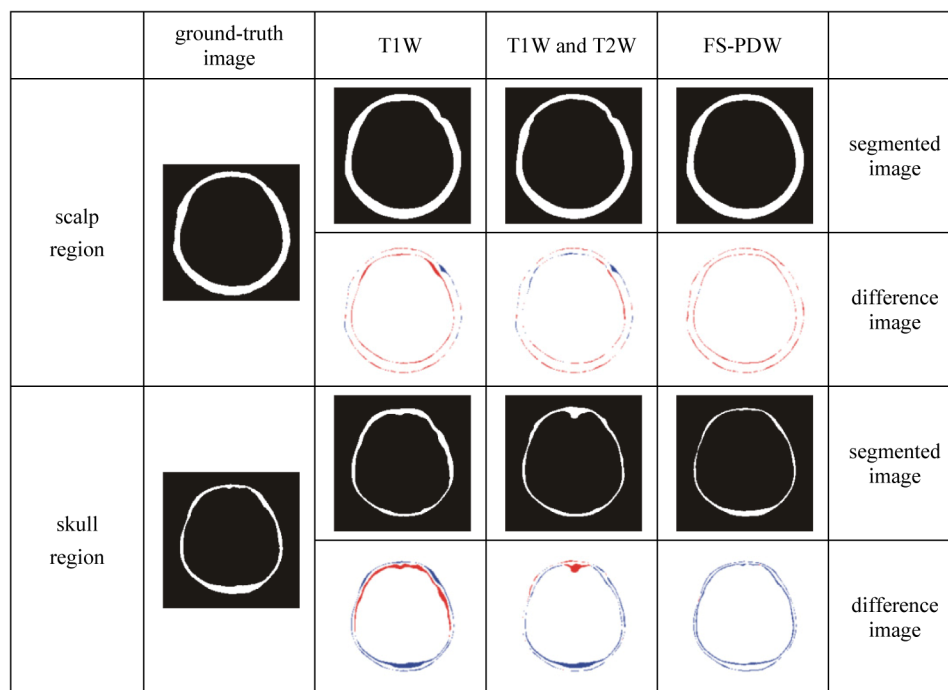


Fig. 7. Scalp and skull regions segmented by BET.








	ground-truth image	T1W	T2W	FIESTA	
CSF region					segmented image
					difference image

Fig. 8. CSF region segmented by FAST.

The Dice coefficients between the images segmented by the BET and the ground truth for the scalp and skull and between the images segmented by the FAST and the ground truth for the CSF are shown in Tables 4 and 5, respectively. The Dice coefficients were calculated for the 136 transaxial plane images in the whole head of a subject and a transaxial plane image for each of the 46 subjects. The segmentations of the superficial tissues from the FS-PDW and FIESTA images by the FSL tools are more accurate than or equivalent to those from the T1W and T2W images despite the fact that the BET and FAST are designed for the T1W and T2W images.

Table 4. Dice coefficient between ground truth and images segmented by BET.

	3D head of a subject			a transaxial plane of 46 subjects		
	T1W	T1W and T2W	FS-PDW	T1W	T1W and T2W	FS-PDW
scalp	0.831	0.910	0.933	0.864 ± 0.048	0.889 ± 0.040	0.905 ± 0.030
skull	0.507	0.777	0.817	0.647 ± 0.114	0.711 ± 0.090	0.778 ± 0.050

Table 5. Dice coefficient between ground truth and images segmented by FAST.

	3D head of a subject			a transaxial plane of 46 subjects		
	T1W	T2W	FIESTA	T1W	T2W	FIESTA
CSF	0.678	0.606	0.690	0.670 ± 0.085	0.676 ± 0.084	0.674 ± 0.080

3.4 Light propagation in head models

Figures 9(a) and 9(b) show two sets of the probe arrangements for the calculation of the partial optical path length and spatial sensitivity profiles. The source and detectors were aligned along a transaxial plane of the head in the probe arrangement 1 whereas the other ones were aligned along a coronal plane in the probe arrangement 2. The detectors were placed from 5 mm to 40 mm at 5-mm intervals.

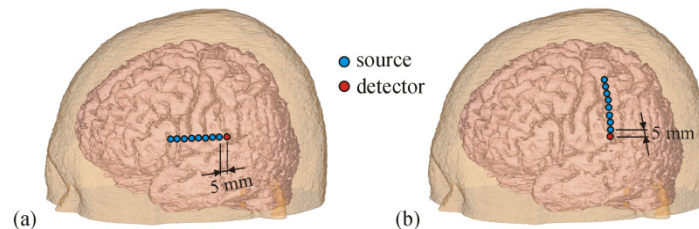


Fig. 9. Probe arrangements: (a) arrangement 1: along transaxial plane, (b) arrangement 2: along coronal plane.

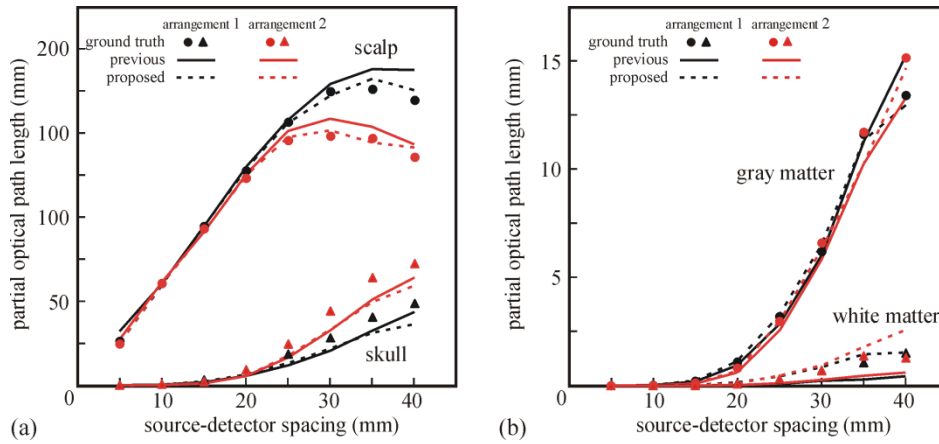


Fig. 10. Partial optical path lengths calculated by the 3D head models: (a) superficial tissues, (b) brain.

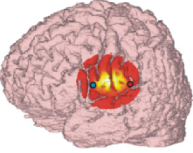
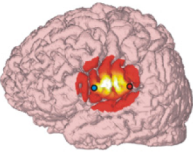
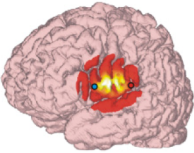
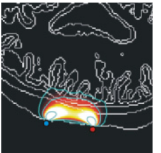
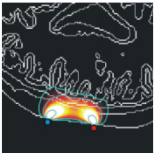
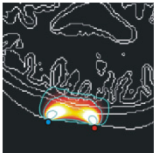
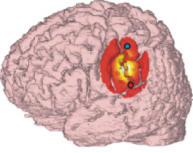
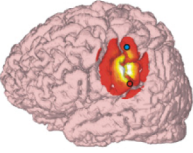
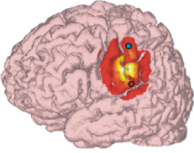
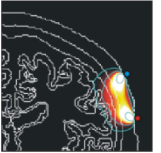
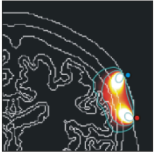
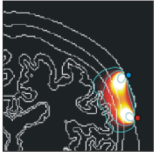
		(a) ground-truth model	(b) previous set of MR images	(c) proposed set of MR images
(1) probe arrangement 1	(i) topographic view	 (a-1-i)	 (b-1-i)	 (c-1-i)
	(ii) tomographic view	 (a-1-ii)	 (b-1-ii)	 (c-1-ii)
(2) probe arrangement 2	(i) topographic view	 (a-2-i)	 (b-2-i)	 (c-2-i)
	(ii) tomographic view	 (a-2-ii)	 (b-2-ii)	 (c-2-ii)

Fig. 11. Topographic and tomographic views of the spatial sensitivity profiles for source-detector spacing of 30 mm: (a) ground-truth model by manual segmentation, (b) model obtained from the previous set of MR images, (c) model obtained from the proposed set of MR images. (1) probe arrangement 1, (2) probe arrangement 2. (i) topographic view of the spatial sensitivity profile on the brain surface, (ii) tomographic view of the spatial sensitivity profile in the plane of the source and detector.

The partial optical path lengths in the superficial tissues (the scalp and skull) and in the brain (the gray matter and white matter) calculated by the 3D head models obtained by the three types segmentations as a function of the source-detector spacing are shown in Figs. 10(a) and 10(b), respectively. The partial optical path lengths estimated by the models obtained by the threshold-based segmentation agree well with that estimated by the ground-truth model obtained by the manual segmentation. Since the threshold-based segmentation tends to underestimate the skull thickness, the partial optical path length in the skull estimated by the models obtained by the threshold-based segmentation is slightly shorter than that estimated by the ground-truth model.

The spatial sensitivity profiles, which indicate the volume of tissue sampled by the source-detector pair of 30-mm spacing in probe arrangements 1 and 2, are shown in Fig. 11. Figures 11(a), 11(b) and 11(c) show the spatial sensitivity profiles estimated from the model obtained by the manual segmentation, by threshold-based segmentation from the T1W and T2W images, and from the FS-PDW, FIESTA and T1W images, respectively. Figures 11(1-i) and 11(1-ii) show topographic and tomographic views of the spatial sensitivity profiles for probe arrangement 1, and Figs. 11(2-i) and 11(2-ii) show those for probe arrangement 2. Both the distribution on the brain and penetration into the brain of the spatial sensitivity estimated by the two models obtained by the threshold-based segmentation are the same and agree with those estimated by the manually segmented ground-truth model.

4. Conclusions

The MR images acquired by the two types of pulse sequences (FS-PDW and FIESTA) were evaluated for the threshold-based segmentation of the superficial tissues of the head to construct the subject-specific head models for DOT. The FS-PDW image is robust to the threshold level and adequate for the threshold-based segmentation of the scalp and skull compared to the T1W and T2W images. The FIESTA image is adequate for the segmentation of the CSF. The segmentations of the superficial tissues from the FS-PDW and FIESTA images by the FSL tools are more accurate than or equivalent to those from the T1W and T2W images despite the fact that the BET and FAST are designed for the T1W and T2W images.

The partial optical path lengths and spatial sensitivity profiles estimated by the head model constructed from the FS-PDW, FIESTA and T1W are almost the same as those estimated by the head model constructed from the T1W and T2W, and they agree with those estimated by the ground-truth model obtained by the manual segmentation.

The advantages of the FS-PDW and FIESTA versus the T2W are not only the robustness to the threshold level and reliability, but also their scan time. The scan time for the FS-PDW is less than one-fifth that for the T2W. The T1W image is essential to construct the subject-specific model because of the contrast between the gray matter and white matter. The FS-PDW image is highly recommended to be complementally used to segment the superficial tissues by not only the threshold-based segmentation, but also the FSL tools. The FIESTA image can be additionally used to improve the segmentation of the CSF region. Even if both the FS-PDW and FIESTA images are acquired, the total scan time is less than one-fourth that for the T2W.

Acknowledgment

A part of this work was supported by JSPS KAKENHI Grant Number 26-5906.